Title Page

Superior anti-corrosion and self-healing bi-functional polymer composite coatings with polydopamine modified mesoporous silica/graphene oxide

Yanqi Ma [a, ‡], Haowei Huang [b, c, ‡], Hongda Zhou [c], Michael Graham [c], James Smith [c], Sihao Li [a], Xinxin Sheng [a, *], Ying Chen[a], Li Zhang [a], Xinya Zhang [b, *], Elena Shchukina [c], Dmitry Shchukin [c]

[a] *Guangdong Provincial Key Laboratory of Functional Soft Condensed Matter, School of Materials and Energy, Guangdong University of Technology, Guangzhou, 510006, China*

[b] *School of Chemistry and Chemical Engineering, Guangdong Provincial Key Lab of Green Chemical Product Technology, South China University of Technology, Guangzhou, 510640, China*

[c] *Stephenson Institute for Renewable Energy, Department of Chemistry, University of Liverpool, Crown Street, Liverpool L69 7ZD, UK*

‡ Yanqi Ma and Haowei Huang contributed equally to this work.

* Corresponding author. E-mail: xinxin.sheng@gdut.edu.cn (X.S.); cexyzh@scut.edu.cn(X.Z.)

Table of Contents (TOCs)

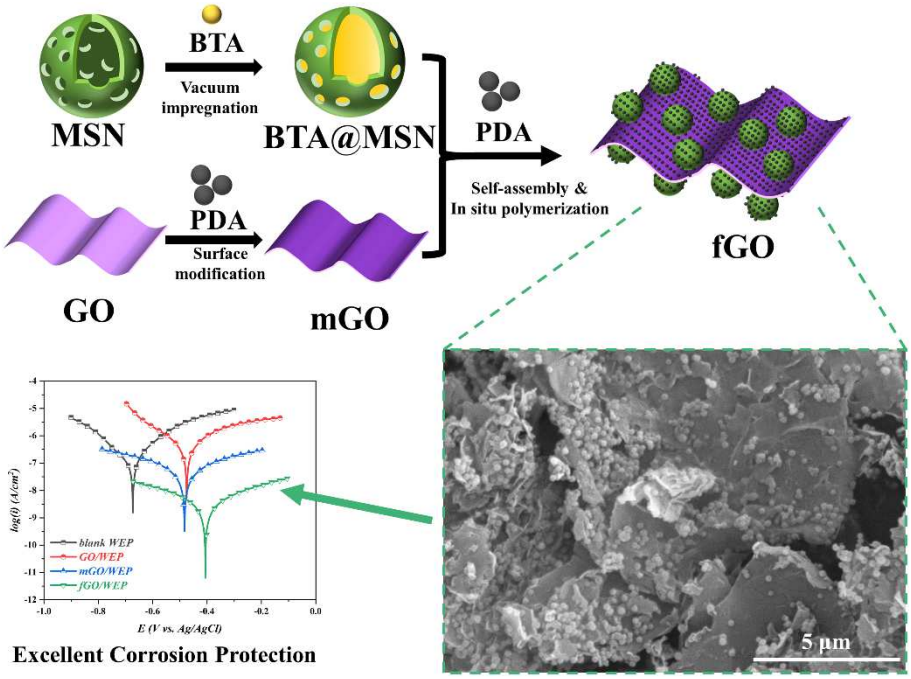

Graphical abstract for submission. On the upper place of the figure, graphene oxide (GO) first was modified by polydopamine (PDA) to obtain modified GO (mGO), and then, benzotriazole-loaded mesoporous silica nanoparticles (BTA@MSNs) are combined on micro scale through the in situ polymerization of polydopamine (PDA), preparing a self-healing bi-functional GO (fGO) for anti-corrosion enhancement of waterborne epoxy (WEP) coatings. On the lower right, it is a scanning electronic image (SEM) of fGO. To the lower left, it is the corrosion protection between blank WEP, GO/WEP, mGO/WEP and fGO/WEP coatings.

Abstract:

In this article, graphene oxide (GO) and benzotriazole-loaded mesoporous silica nanoparticles (BTA/MSNs) are combined on micro scale through the in situ polymerization of polydopamine (PDA), preparing a self-healing bi-functional GO (fGO) used as nano-fillers for anti-corrosion enhancement of waterborne epoxy (WEP) coatings. Scanning electronic microscope (SEM) images show that the BTA/MSNs are uniformly distributed on the surface of high aspect ratio GO nanosheets to endow GO nanocontainer characteristics. UV-vis profiles demonstrate that fGO has pH-controlled release function. Modulus at lowest frequency is generally used for comparing the corrosion resistance of organic coatings. Modulus at lowest frequency (1.42×10^{7} $\Omega\cdot cm^{2}$) after 30 days immersion in 3.5 wt.% NaCl solution revealed 2 orders of magnitude higher that of blank WEP (8.22×10^{-3} $\Omega\cdot cm^{2}$). With artificial cracks on its coatings, fGO/WEP had no obvious rust compared with blank WEP after 240 hours of immersion. We anticipate that self-healing and physical barrier bi-functional nanocontainers improve the traditional anticorrosion coating efficiency with better, longer-lasting performance for shipping, oil drilling or bridge maintenance.

Keywords: mesoporous silica; graphene oxide; corrosion inhibitor; nanocontainer; waterborne epoxy coatings

1. Introduction

Anticorrosive polymeric coatings are the most widely used and most effective for protecting metals from environmental corrosion [1]. As environmental awareness increases, the market share of water-based epoxy (WEP) anticorrosive coatings continues to rise [2, 3]. However, shrinkage, defects and micro-cracks are likely to appear inside WEP after film formation due to the inherent characteristics of water-based coatings [4, 5]. To enhance barrier performance, novel two-dimensional (2D) ultra-thin nanomaterials, especially graphene, were introduced into the WEP coatings [6, 7]. Graphene has good chemical stability and perfect impermeability against corrosive ions, water and oxygen [8, 9]. To further increase anti-corrosion properties, the graphene surface was modified by covalently or non-covalently grafted molecules to reduce the interface incompatibility between graphene and polymer matrix [10, 11].

Commonly used surface modification methods for graphene include organic molecular grafting [12], polymer encapsulation [13], surfactant adsorption [14] and inorganic nanoparticles decoration (Silica, Zirconia, Alumina, Carbon nanotubes, etc.) [15, 16]. Among them, the decoration of inorganic nanoparticles has outstanding advantages: it can not only reduce the agglomeration between graphene nanosheets through steric repulsion between nanoparticles [17, 18], but also involves properties of nanoparticles to attain graphene additional functionality. This includes inhibiting corrosion-promotion activity of graphene [19], corrosion protection of photo-generated cathode anticorrosion [20], wear resistance [21], superhydrophobicity [22], anti-bacterial properties [23], flame-retardancy [24] and self-healing ability [25].

Mesoporous silica nanoparticles (MSNs) are ideal nanocontainers with a three-dimensional (3D) topological structure and high chemical and thermal stability [26]. Since their discovery, MSNs have been widely used in drug release [27], phase change energy storage [28, 29], anti-fouling [30], catalytic [31] and corrosion inhibitor loading [32]. Encapsulating corrosion inhibitors into MSNs can effectively prevent the corrosion inhibitor from adversely affecting the polymer coating curing process [33, 34] and achieve long-term environmentally responsive self-healing behaviour [35, 36]. The combination of graphene and MSNs is an innovative attempt to couple active

(controlled release) anticorrosion and passive defense (physical barrier) in one composite coating.

Li et al. [37] attached amine-functionalized MSNs onto GO via a ring-opening reaction at 110 °C for 4 hours. Then, the corrosion inhibitor (tannic acid, TA) was loaded into it by vacuum impregnation to obtain TA-loaded GO nanocontainers (TA-GO). Compared with MSNs coating, TA-GO coating exhibits self-healing ability and can resist failure caused by alternating changes in hydrostatic pressure. Wang et al. [38] used cetyltrimethylammonium chloride (CTAC) as an auxiliary molecule to synthesize MSNs on graphene oxide (GO) in situ, obtaining $mSiO_2$/GO nanocontainers with a sandwich structure. Subsequently, benzotriazole (BTA) molecules were loaded into the $mSiO_2$/GO nanocontainers for corrosion protection of copper and steel. The nanocomposite coating showed excellent anticorrosion performance. Yu et al. [39] fabricated functionalized GO (fGS) by first in situ synthesizing BTA-loaded ordered MSNs on it and then modifying the composite with aminopropyl triethoxysilane (APTES). Aminosilane functionalization improves the dispersion stability of fGS and provide BTA/fGS with stimulus-response release under alkaline conditions.

Polydopamine (PDA) is an environmentally friendly chemical modifier inspired by the strong adhesion of mussels to rocks [40]. It can be deposited on the surface of many materials, including steel [41], biomass [42], plastics [43] and nanoparticles [44]. Nanosized PDA polymer particles have strong physical adsorption on the surface of the substrate via catechol and amine hydrogen bonding [45, 46]. Based on this particular properties, PDA can be considered as a nano-sized adhesive [47]. In our previous work, PDA was used as a binder to combine GO and boron nitride (h-BN) in one pot to obtain h-BN-rGO@PDA nanohybrids with excellent corrosion protection properties [48]. In addition, Qian et al. [49] discovered that the use of PDA to encapsulate MSNs can achieve a controlled release of BTA loaded in MSNs when pH is lower than 5, which is beneficial for preparing anticorrosive nanocomposite coating with sustainable long term effect.

Herein, we took the advantages of the self-polymerization reaction of PDA to combine GO and MSNs that have been vacuum-loaded with BTA in a pot to obtain a

MSNs-functionalized GO (fGO) nanocomposite with both self-healing and barrier function, and load the nanocomposite particles into a WEP coating as anticorrosive additive. In order to characterize the structure of fGO, field emission high resolution microscope (FESEM), TEM, thermogravimetric analysis (TGA), attenuated total reflection-Fourier transform infrared spectra (ATR-FTIR) and X-ray diffractometer (XRD) were adopted. UV–visible spectrophotometer was used to study the release dynamic of BTA from fGO. Electrochemical impedance spectroscopy (EIS) and potentiodynamic polarization were taken to investigated the anticorrosion performance of fGO/WEP composite coating. We anticipate that the binder and release-controlling effect of PDA can provide inspiration for future green materials.

2. Experimental

The fabrication process is described in Figure 1. First, MSNs were synthesized via a template-assisted hydrolysis method. And then, BTA was loaded into MSNs by vacuum impregnation, producing MSNs-encapsulated BTA (BTA@MSNs). At the same time, GO was modified by PDA, resulting a PDA modified GO (mGO). mGO and BTA@MSNs were placed into a pot where PDA had its in situ polymerization. Finally, MSNs-functionalized GO (fGO) was fabricated. More details of the experimental procedures can be found in the Supporting Information.

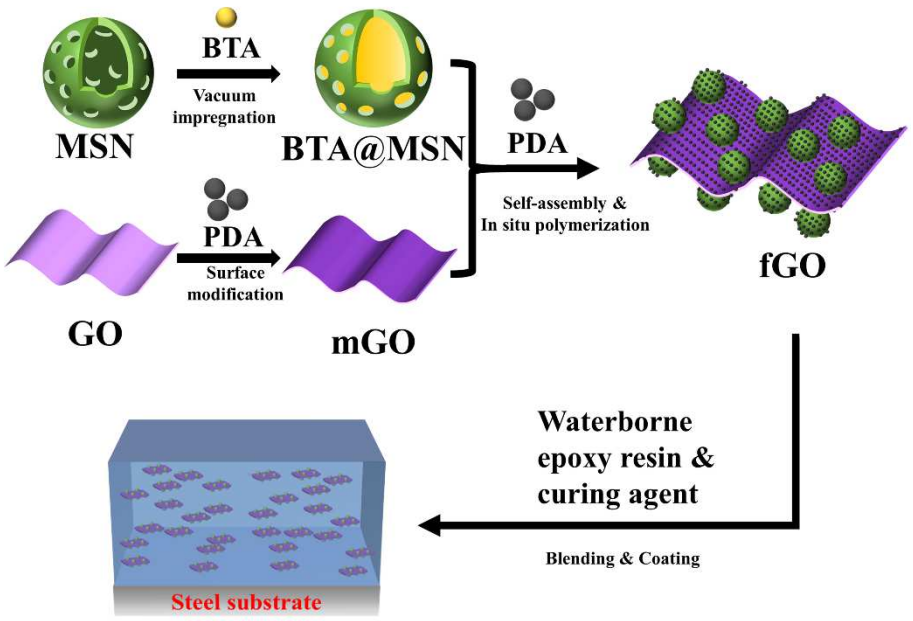

Figure 1. Experimental scheme showing fGO preparation using GO and MSNs as raw materials and incorporation of fGO into the composite WEP coating. Please refer to Supporting Information Section for experimental details.

3. Results and discussion

3.1 The basic characterization of fGO

Scanning electron microscopy (SEM) and transmission electron microscopy (TEM) were used to observe the morphology of MSNs, GO, mGO, and fGO. As shown in Figure 2a and 2b, MSNs are smooth spherical nanoparticles with mesoporous structure. Dynamic light scattering (DLS, Figure S1) shows the average MSN particle size of 173.6 nm. Commercial grade GO has a 2D structure with a smooth surface and a super large aspect ratio of about 4000 (Figure 2c and 2d). BET isotherms (Figure S2) confirm MSNs have a very large specific surface area (1292.96 m^2/g), making them ideal for loading with active materials such as BTA. GO has an extremely small specific surface area (4.62 m^2/g) , but can be used in conjunction with MSNs. After PDA processing, the surface of mGO becomes rougher and wrinkles become more obvious (Figure 2e and 2f). This is because unsaturated bonds on the GO surface are reduced during the oxygen-consuming PDA formation [48]. The rough mGO surface provides more

attachment sites for MSNs than smooth GO. There are many evenly distributed MSNs (tiny particles) on the surface of fGO (Figures 2g, 2h), indicating that resulted fGO has the properties of MSNs' nanocontainers and GO's high aspect ratio.

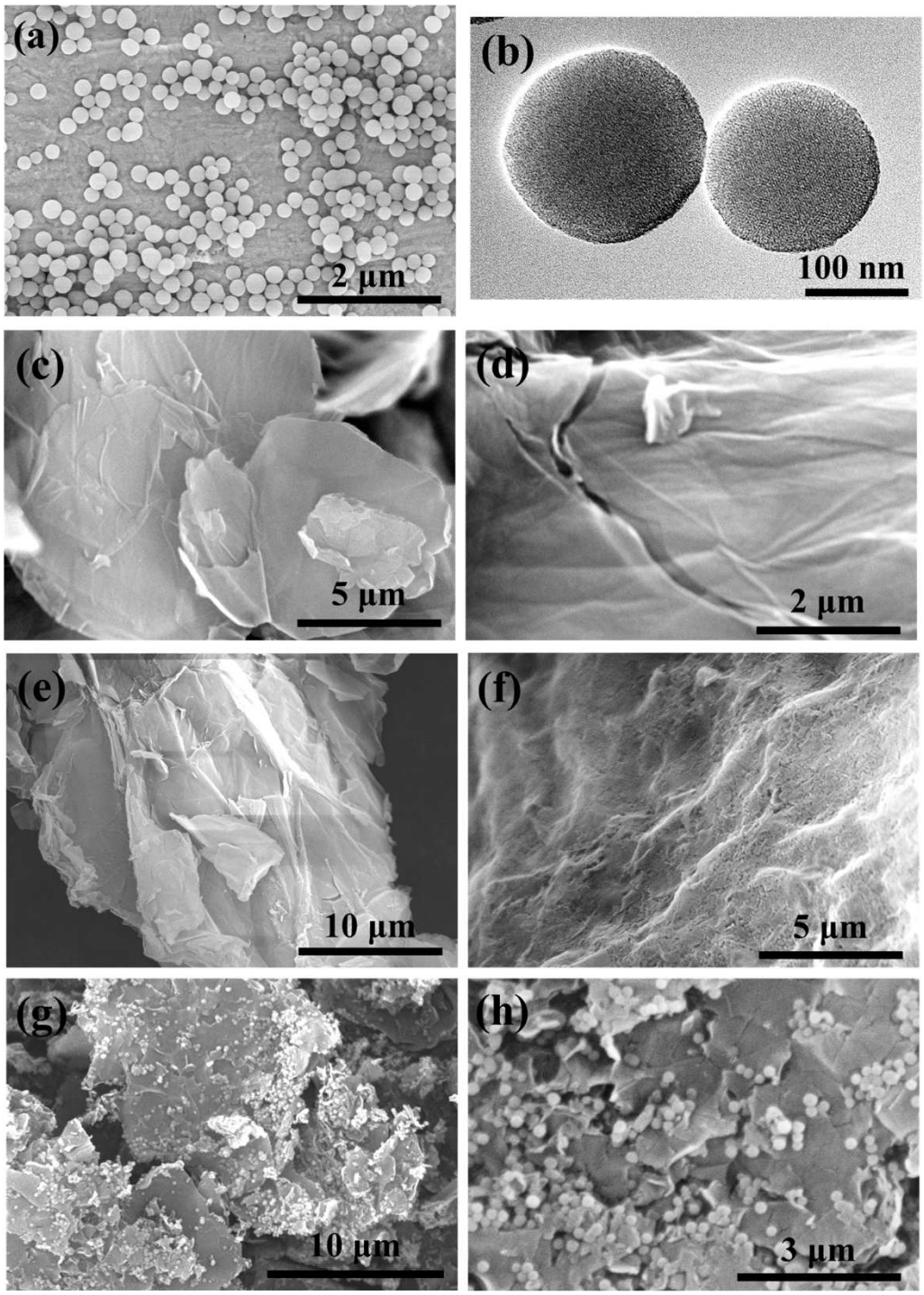

Figure 2. SEM images of (a) MSNs, (c, d) GO, (e, f) mGO, and (g, h) fGO; (b) TEM image of MSNs.

Figure 3a shows the infrared spectra of MSNs, GO, mGO, and fGO. For MSNs, 3451 cm^{-1} and 1630 cm^{-1} are related to the stretching and bending vibration peaks of physically absorbed water; 1077 cm^{-1}, 803 cm^{-1} and 452 cm^{-1} correspond to the asymmetric vibration, symmetrical stretching and bending of Si-O-Si, respectively [27, 32]. In GO, the absorption peaks at 3411 cm^{-1}, 1732 cm^{-1}, 1634 cm^{-1}, 1391 cm^{-1}, and 1082 cm^{-1} are attributed to -OH, carboxyl C=O, aromatic C=C, C-OH, C-O-C epoxide, respectively [12, 13, 50]. After being modified by PDA, there are many new absorption peaks on mGO (for example, stretching of N-H at 3379 cm^{-1}, shearing of N-H at 1592 cm^{-1}, and stretching of C-N at 1357 cm^{-1}) [51-53]. The infrared spectrum of fGO has Si-O-Si blending peaks (406 cm^{-1}) that mGO does not have. In addition, the intensities of N-H absorption peaks related to mGO on fGO show a certain degree of reinforcement indicating that the PDA content of fGO is increased after using PDA's polymerization to bind mGO and MSNs. The above phenomena show that mGO and MSNs are successfully deposited to fGO surface.

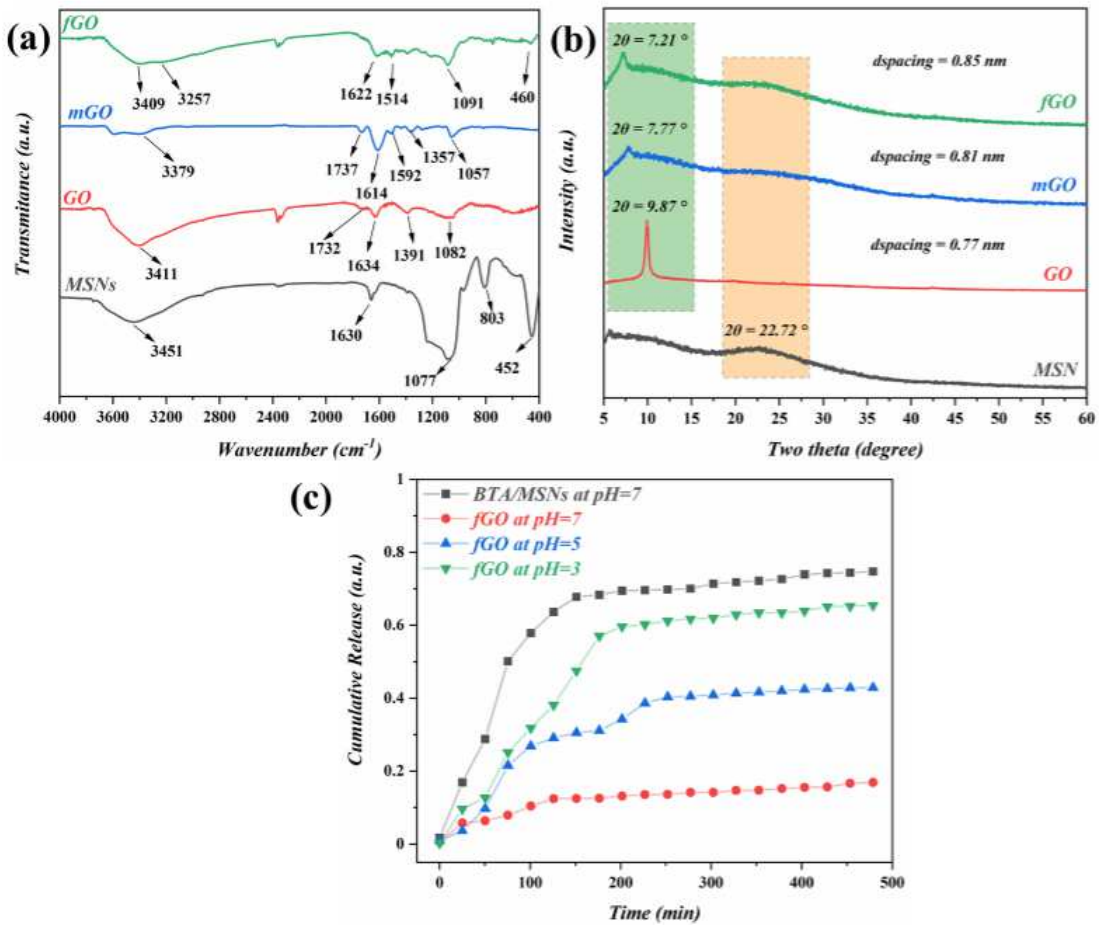

Figure 3. (a) FTIR spectra, (b) XRD patterns of MSNs, GO, mGO, and fGO; (c) release profiles of BTA in MSNs or fGO when facing different pH environments.

We performed wide-angle XRD ray diffraction of MSNs, GO, mGO, and fGO, as shown in Figure 3b. MSNs have a broad peak at 2θ=22.72°, which is caused by the amorphous structure of silica (JCPDS NO: 29-0085) [54]. For GO, mGO, and fGO, diffraction peaks corresponding to the GO crystal plane (001) appear at low angles (2θ<10°). According to the Bragg equation [13], we can calculate the d-spacing of GO, mGO, and fGO is 0.77 nm, 0.81 nm, and 0.85 nm, respectively. The increase of d-spacing indicates that GO was successfully intercalated by PDA and MSNs, which can effectively reduce the agglomeration inside mGO and fGO, and greatly facilitate its dispersion in the resin matrix [55]. At the same time, the diffraction peaks of the (001) plane of mGO and fGO are broader than GO, indicating that the modification resulted in a decrease in the integrity of the crystal structure of GO and an increase in disorder.

In addition, the characteristic peak of MSNs (approximately at 2θ=22.72°) was also found in fGO. It shows that fGO is a hybrid nanomaterial composed of mGO and MSNs.

Figure S3 reveals TGA curves of BTA, GO, MSNs, mGO and fGO. It can be seen that BTA, as a small organic molecule, begins to thermally decompose at around 204 °C and is completely degraded at around 325 °C. For MSNs, there is a period of weight loss (about 3.5%) before 120 °C. This is due to the moisture absorbed inside its porous structure. However, the weight of MSNs (94.89%) remained stable during the subsequent heating process. After loading BTA, BTA/MSNs also began to decompose at around 204 °C and reached equilibrium at around 325 °C with a weight loss of 47.54%. Through the difference between the weight loss values of BTA/MSNs and MSNs, the load of BTA in MSNs is 40.29%. Pure GO decomposes at around 372 °C and reaches the maximum degradation (95.17%) at 735.6 °C. Since fGO is loaded with BTA, its onset temperature (approximately 227°C) is lower than that of GO, but its temperature corresponding to the maximum degradation value (81.92wt.%) (approximately 739°C) is slightly higher than that of GO. The incorporation of inorganic materials (MSNs) in fGO imparts good thermal stability of the composite. Calculating the residual value between fGO and GO. The proportion of MSNs in fGO is 14.42%. In total, the load of BTA in fGO is 5.28%.

As shown in Figure 3d, BTA rapidly releases from MSNs rapidly in a neutral environment (pH 7) and reached a release equilibrium (about 70 %) at t=150 min. This is due to the open porous structure of MSNs. Such a rapid release results in BTA wasting and the adverse effect of the released free BTA on the curing of the WEP coating. Therefore, we deposited PDA to modify the surface of MSNs. With PDA layer, the release of BTA from fGO at pH 7 is greatly reduced to 10 % by negatively charged catechol and indole functional groups of PDA, which prevent the release of BTA due to electrostatic repulsion. [49, 51]. At pH 3, the release speed is significantly increased due to the autonomous fGO response, a demonstration of the smart nanocontainer response to local pH.

3.2 The characterization of fGO/WEP composite coating

3.2.1 The distribution of fGO in WEP

Figure 4 exhibits the SEM images of cross-section of blank WEP, GO/WEP, mGO/WEP and fGO/WEP produced by liquid nitrogen quenching. As shown in Figure 4a, the surface of the blank WEP coating is relatively smooth, but there are many visible micropores and cracks due to the inherent defects of the water-based resin after curing. The cross-sections of the other three samples are rougher than the blank WEP, which is caused by the rigidity increase after the addition of nanomaterials [12, 44, 52]. For GO/WEP in Figure 4b, there are large agglomerates caused by the lipophilic incompatibility between GO and WEP. After PDA modification of GO, there is no apparent agglomeration on the SEM image of mGO/WEP (Figure 4c). Scattered nanospheres were found in the cross section of fGO/WEP (Figure 4d), indicating that MSNs can be uniformly dispersed in the WEP matrix after being loaded on GO. At the same time, fGO is affected by the grafting of MSNs, causing the roughness of fGO/WEP to increase compared with mGO/WEP.

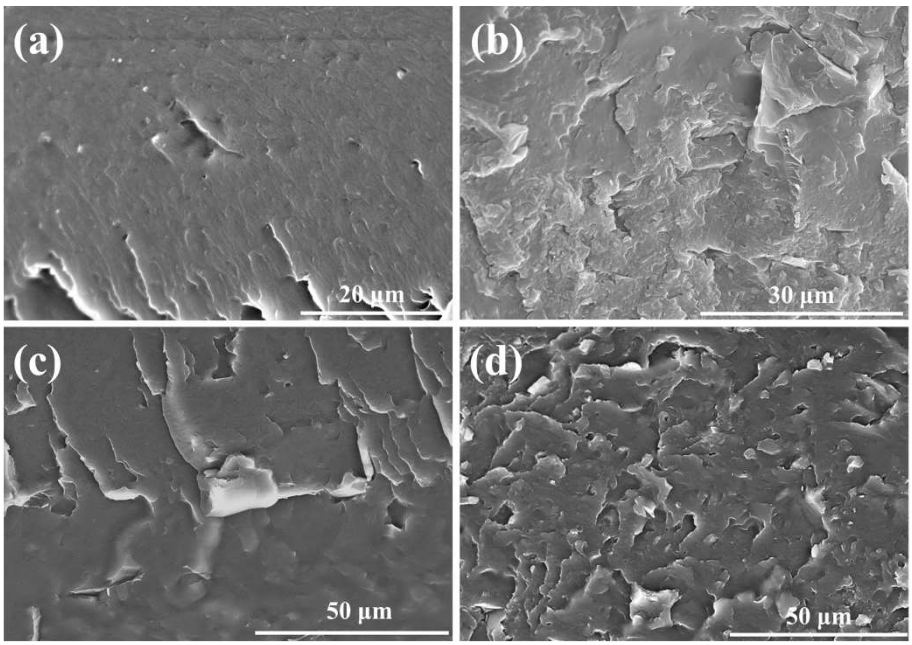

Figure 4. SEM images of cross-section of (a) blank WEP, (b) GO/WEP, (c) mGO/WEP and (d) fGO/WEP produced by liquid nitrogen quenching.

3.2.2 Anticorrosion performance of composite coatings

In order to study passive anti-corrosion ability of fGO/WEP coating, we carried out

EIS test (Figure 5) and Tafel test (Figure S4) for all coatings in NaCl solution (pH 7, 3.5wt%) for up to 30 days.

Figure 5 displays resistance performance for the composite coatings over time. For the blank WEP in Figure 5a, the Bode modulus decreases with the time, and the low-frequency platform length is getting longer. It demonstrates that the WEP coating suffered severe corrosion damage after 30 days of immersion [8]. The Bode phase angle of WEP is constantly shifting to high frequencies (Figure 5b), which indicates that the adhesion of the blank WEP coating is significantly reduced resulting in a decline in barrier performance [5]. GO/WEP (Figure 5c and 5d) also experienced a decline trend similar to the blank WEP but it decreased faster. After immersion on the 4th day, there was a worse decline than WEP due (i) the incompatibility of GO and WEP increasing internal defects in the coating as shown by SEM in Figure 4 and (ii) hydrophilic GO easily absorbs corrosive media. After modification with PDA, mGO/WEP has more advantages than GO/WEP in terms of initial value, downward trend and final value (Figure 5e and Figure 5f). Modification with PDA improves dispersion of mGO in WEP. Large aspect ratio of mGO reduces coating porisity, while the catechol group of PDA demonstrates good adhesion to metal substrate [44, 47]. fGO/WEP exhibits the most stable Bode modulus and lowest Bode phase angle over 30 days (Figure 5g and Figure 5h). This may be due to the fact that the d-spacing of fGO is larger than that of mGO, as suggested by XRD. Therefore, fGO can be better dispersed thus improving the barrier performance. The surface modification with PDA similar to mGO provides good metal adhesion for fGO/WEP.

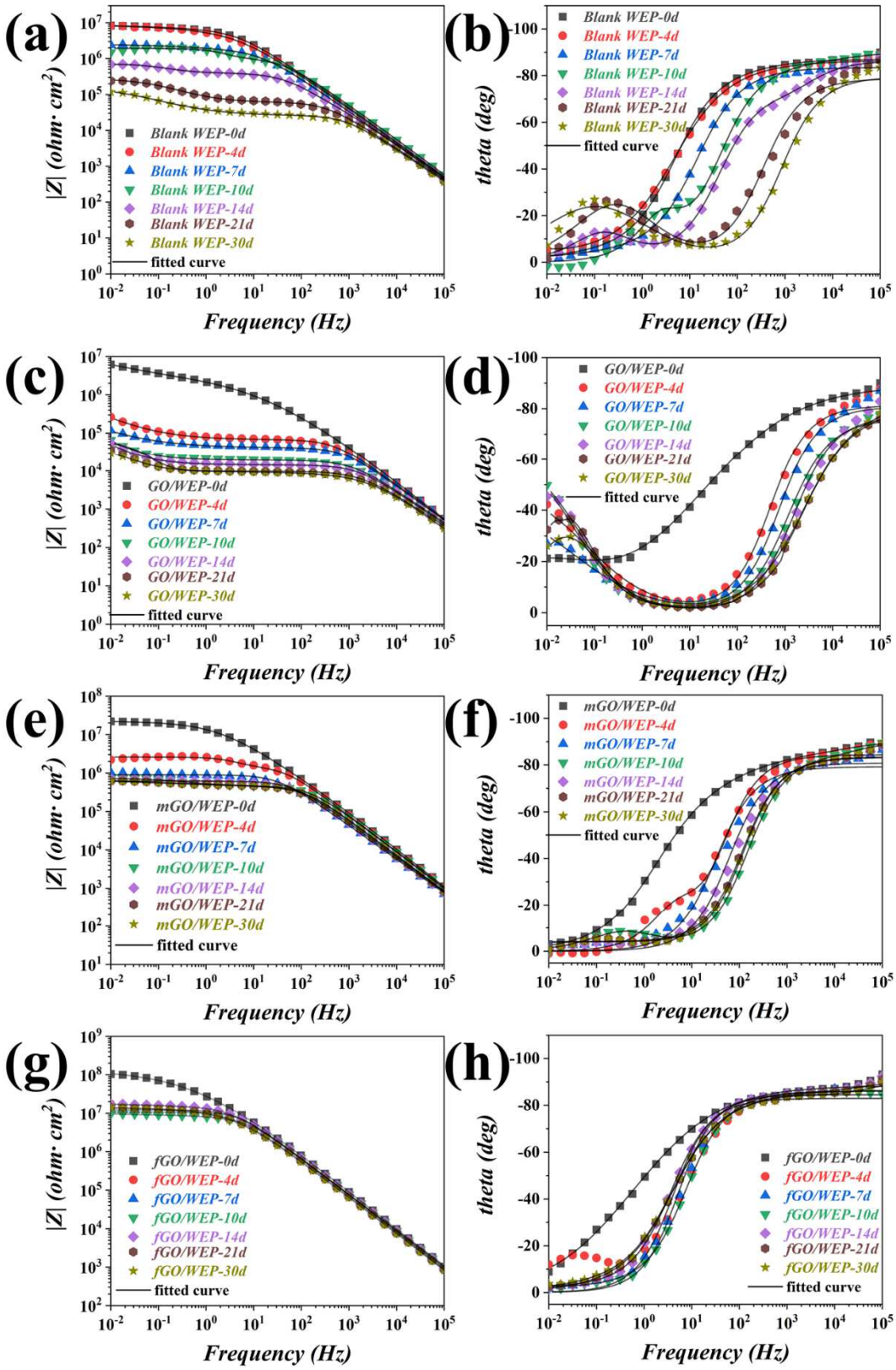

Figure 5. The Bode modulus of (a) blank WEP, (b) GO/WEP, (c) mGO/WEP and (d) fGO/WEP and Bode phase angle of (e) blank WEP, (f) GO/WEP, (g) mGO/WEP and (h) fGO/WEP.

The influence of immersion time on the anti-corrosion performance of the composite coating is described in Figure 6. As seen in Figure 6a, the lowest frequency modulus $|Z_{0.01Hz}|$ values of the four coating samples all show a downward trend with increased immersion time. The value of $|Z_{0.01Hz}|$ tested on the 30th day is as follows, fGO/WEP (1.42×10^7 Ω·cm^2) > mGO/WEP (6.10×10^5 Ω·cm^2) > blank WEP (1.17×10^5 Ω·cm^2) > GO/WEP (2.91×10^4 Ω·cm^2). The lowest modulus value of fGO/WEP after 30 days is more than 2 orders of magnitude of the blank coating. Therefore, adding even small amounts (1 wt.%) of fGO to WEP imparts excellent anti-corrosion barrier performance.

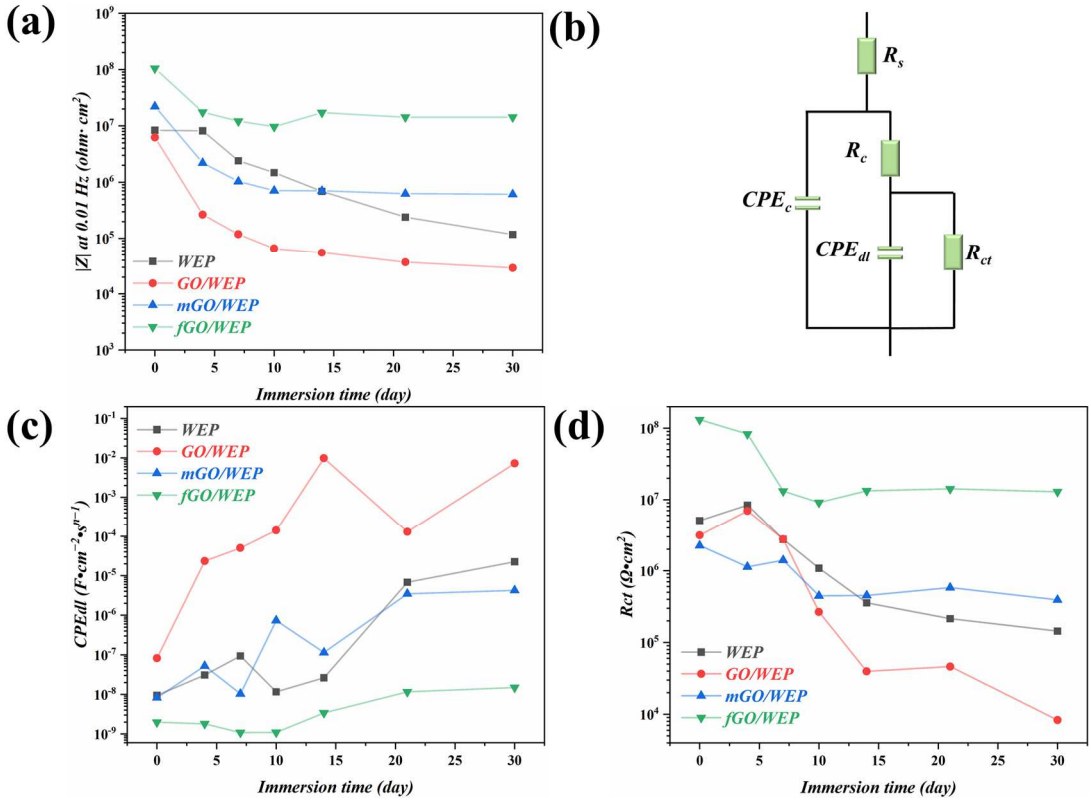

Figure 6. (a) $|Z_{0.01Hz}|$, (c) CPE_{dl} and (d) R_{ct} of MSNs, GO, mGO, and fGO during immersion in NaCl soultion; (b) The EEC used for simulating EIS data.

We used the equivalent electric circuit (EEC) shown in Figure 6b to fit the above-mentioned EIS data. R_s represents the solution resistance, R_c stands for the coating resistance; R_{ct} is the charge transfer resistance; CPE_c simulates the non-constant phase

capacitance of the coating; CPE_{dl} is the non-constant phase capacitance of the double layer. The relevant specific fitting data are presented in Table S1. From the high degree of overlap between the gray fitting line in Figure 5 and the real data (the scatter points), it can be known that the fitted EECs are reliable for explanation of EIS.

Dependence of CPE_{dl} and R_{ct} vs. immersion time is shown in Figures 6c and 6d. CPE_{dl} represents the thickness of the electric double layer at the interface between the coating and the metal [49]. The larger the value of CPE_{dl}, the greater is the degree of adhesion drop caused by the penetration of the corrosive medium to the coating/metal interface. Figure 6c shows that fGO/WEP has the smallest value of CPE_{dl}, indicating the best adhesion to the metal substrate. R_{ct} is an indicator of the corrosion proctection offered by the coating [12, 13]. The fGO/WEP in Figure 6d has the highest R_{ct} value compared to other samples during 30 days confirming effective prevention of corrosion of metal substrates.

As shown in Figure S4, the corrosion potentials (E) of fGO/WEO and mGO/WEP are both positive than blank WEP. Therefore, it can be inferred that PDA-modified materials have better stability in corrosive environments. After 30 days of immersion, blank WEP, GO/WEP, mGO/WEP and fGO/WEP were tested by Tafel method to calculate the annual corrosion rate (CR)[13]:

$$CR = \frac{kM_m I_{\text{corr}}}{\rho_m}$$

According to the data in Table S2, the value of CR has changed significantly: fGO/WEP (1.82×10^{-4} mpy) < mGO/WEP (2.78×10^{-3} mpy) < blank WEP (8.22×10^{-3} mpy) < GO/WEP (3.00×10^{-2} mpy). The CR value of fGO/WEP is more than order of magnitude lower than the blank WEP, further illustrating the impressive corrosion protection ability of fGO fillers.

3.2.3 The self-healing performance of scratched composite coatings

In order to study the active (self-healing) anti-corrosion activity, we made two crossing scratches on the surface of all the coatings, leaving the metal directly exposed to a corrosive environment for 240 hours.

Figure 7 displays a clear difference between the scratched coatings. The blank WEP coating has obvious yellow rust left along the scratches, and black corrosion products appear at the intersection. It shows that the blank coating offers minimal corrosion protection. The accumulation of black corrosion products on the GO/WEP coating is more serious than blank one, and corrosion products are also produced in places where there are no scratches. It indicates that the overall protection performance of GO/WEP is inferior even to blank WEP. mGO/WEP also has black corrosion products, but only along the scratched area. This shows the mGO fillers impart good barrier corrosion protection, but with little self-healing ability in damaged area. fGO/WEP demonstrates the best performance combining barrier corrosion protection of the pristine coating with self-healing functionality in the cracks. This is realised with a similar macroscopic appearance after 240 hours of exposure to corrosive environment. In order to better study the self-healing phenomenon, the intersection of the scratches of the coating was monitored by SEM. For blank WEP, a large amount of continuous ridge-like dense rust appears on the surface of the steel substrate. Many loose corrosion products can be found on GO/WEP sample. It indicates that GO/WEP's corrosion products are transformed, resulting in a higher corrosion degree than blank WEP. mGO/WEP has only sporadic corrosion products. The fGO/WEP's metal surface has only straight and clear rough surfaces and no corrosion products were found.

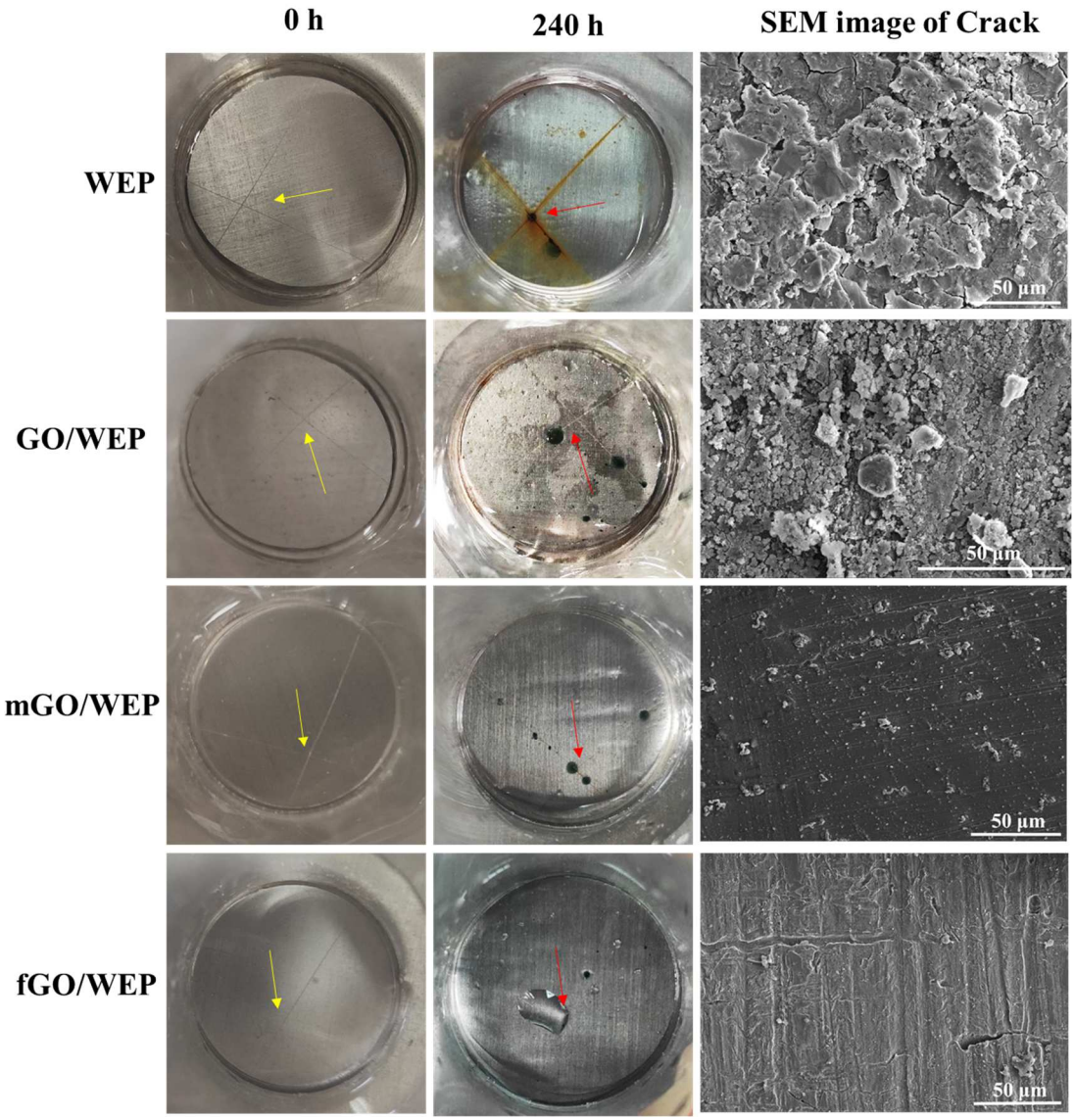

Figure 7. Visual images (left) of blank WEP, GO/WEP, mGO/WEP and fGO/WEP before and after immersion in 3.5 wt.% NaCl solution for 240 hours. The yellow/red arrows show the intersection of the two scratches made with a scalpel. The area of the coating exposed to the corrosive environment is 7.07 cm^2. SEM images (right) of the intersection of the scratches of blank WEP, GO/WEP, mGO/WEP and fGO/WEP after immersion.

In addition to qualitatively analysis of the amount of corrosion products, we also performed a SEM-EDS test of the elemental composition of the corrosion products (Figure 8) for quantitative analysis. Blank WEP rust in Figure 8a is 47.7% oxygen, 0.5% sodium, 7.8% chlorine and 43.8 iron. In GO/WEP (Figure 8b), the oxygen and chlorine

content decreased to 37.9% and 4.4% but the iron content increased to 57.5%, indicating that the rust has been transformed to a more advanced form and more metal (iron) on the substrate surface is consumed. However, both the oxygen (10.2%) and chlorine (0.7%) decreased sharply in mGO/WEP (Figure 8c). The oxygen (4.6%) and chlorine (0.1%) content of fGO/WEP (Figure 8d) is much lower than blank WEP. It is confirmed that the iron sheet covered by fGO/WEP has good integrity. The microscopic behaviour is consistent with the macroscale observations in Figure 7.

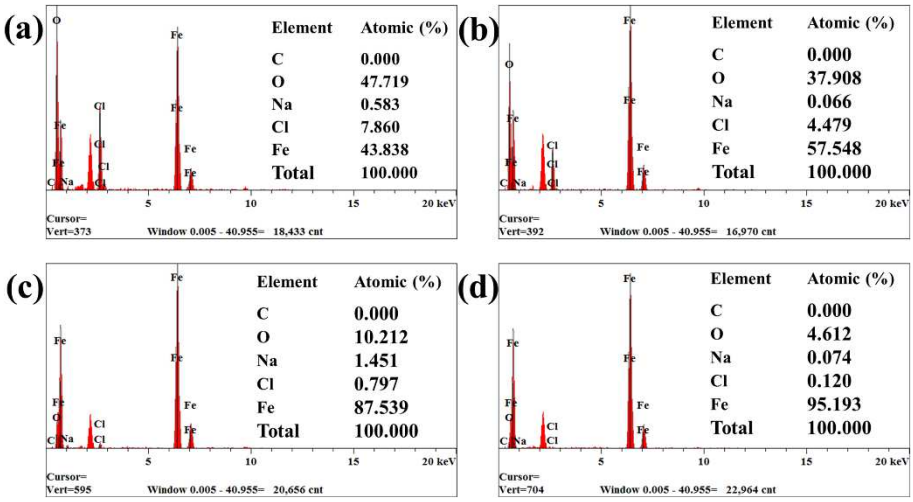

Figure 8. SEM-EDS result of the intersection of the scratches of (a) blank WEP, (b) GO/WEP, (c) mGO/WEP and (d) fGO/WEP.

3.2.4 The anticorrosive mechanism of fGO/WEP

Based on the above experimental data and analysis, the anti-corrosion mechanism of fGO/WEP compared to blank WEP is proposed in Figure 9. Because the blank WEP coating has many micropores and micro cracks, the corrosive medium is free to attack metal surface. Therefore, the risk of metal corrosion is high. The cracks of the blank WEP accelerate damage to the metal surface by corrosive medium. Adding fGO fillers to WEP has two distinct advantages. It enhances the barrier ability of WEP when the coating is intact by providing a "labyrinth effect" that extends the penetration path for corrosive media through its random but non-agglomerated distribution inside the coating. At the same time, fGO releases the corrosion inhibitor (BTA) by responding to the pH change of the corrosive microenvironment when the coating is scratched. BTA reacts with exposed metal surface to increase the corrosion potential of metals and thus

inhibit corrosion. In summary, fGO is a new generation nano container with active and passive anti-corrosion functions.

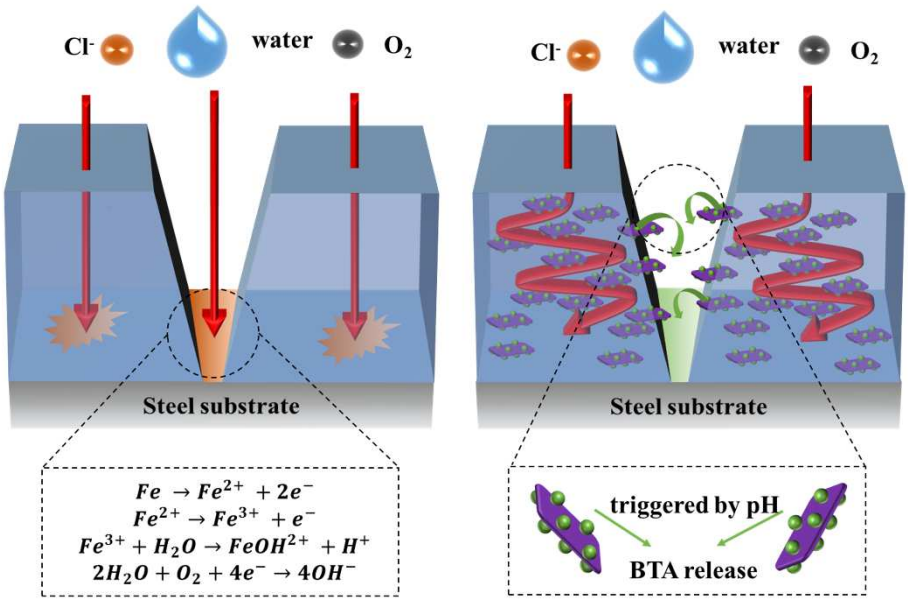

Figure 9. Schematic presentation of the anticorrosion performance of blank WEP (left) and fGO/WEP (right).

4. Conclusion

In this article, we used the in-situ polymerization of PDA to prepare benzotriazole (BTA)-loaded MSN-GO@PDA (fGO). PDA modifes GO to provide more adsorption sites for the binding of GO to MSNs and wrap MSNs to control BTA release in response to pH changes of the environment. FTIR/XRD/SEM results show that GO and MSNs have been successfully combined. TGA demonstrated the loading of BTA in fGO is of 5.28 wt.%. UV-vis measurements showed BTA release from fGO under acidic condition pH<5. PDA is beneficial to the dispersion of active nanocontainers in WEP as confirmed by SEM of the cross-section of the coatings. Electrochemical impedance measurements revealed lowest frequency modulus $|Z_{0.01Hz}|$ value (1.42×10^{7} Ω·cm^2) and annual corrosion rate (1.82×10^{-4} mpy) of fGO/WEP were 2 orders of magnitude higher and 1 order of magnitude lower than that of blank WEP (8.22×10^{-3} Ω·cm^2, 8.22×10^{-3} mpy), respectively. fGO/WEP has good passive barrier anticorrosion performance. In the self-healing test of scratches, the corrosion products on the surface of the metal substrate protected by fGO/WEP are less than 10% of the blank WEP. It is confirmed

that fGO/WEP has self-healing anti-corrosion ability. Nanocontainers with both self-healing and physical barrier anticorrosion functionalities can be used for protection of ships, offshore facilities, bridges and 5G base stations because they do not only meet the anticorrosion requirements of a complete coating under normal and causal conditions, but also respond to extreme conditions of coating damage with autonomic self-healing response.

Associated content

Supporting information

Author information

Corresponding authors

*E-mail: xinxin.sheng@gdut.edu.cn (X.S.); cexyzh@scut.edu.cn(X.Z.)

Note

The authors declare no competing financial interest.

Acknowledgements

This work was supported by the National Natural Science Foundation of China (Grant No. 51908031). Haowei Huang thanks the China Scholarship Council for a graduate fellowship (201906150013). Y. C. acknowledges the support from Guangdong Special Support Program (Grant No. 2017TX04N371). ES and DS thank ERC Enercapsule project (647969) and Royal Society project IEC\R2\202163.

References

[1] M. Davoodi, E. Ghasemi, B. Ramezanzadeh, M. Mahdavian, Designing a zinc-encapsulated Feldspar as a unique rock-forming tectosilicate nanocontainer in the epoxy coating; improving the robust barrier and self-healing anti-corrosion properties, Construction and Building Materials, 243 (2020) 118215.

[2] D.C. Webster, R.A. Ryntz, Pigments, Paints, Polymer Coatings, Lacquers, and Printing Inks, in: Handbook of Industrial Chemistry and Biotechnology, Springer, 2017, pp. 805-822.

[3] M. Cui, S. Ren, J. Chen, S. Liu, G. Zhang, H. Zhao, L. Wang, Q. Xue, Anticorrosive performance of waterborne epoxy coatings containing water-dispersible hexagonal boron nitride (h-BN) nanosheets, Applied Surface Science, 397 (2017) 77-86.

[4] Y. Wu, Y. He, C. Chen, F. Zhong, H. Li, J. Chen, T. Zhou, Non-covalently functionalized boron nitride by graphene oxide for anticorrosive reinforcement of water-borne epoxy coating, Colloids and Surfaces A: Physicochemical and Engineering Aspects, 587 (2020) 124337.

[5] Y. Tian, Y. Xie, F. Dai, H. Huang, L. Zhong, X. Zhang, Ammonium-grafted graphene oxide for enhanced corrosion resistance of waterborne epoxy coatings, Surface and Coatings Technology, 383 (2020) 125227.

[6] C. Chen, Y. He, G. Xiao, F. Zhong, H. Li, Y. Wu, J. Chen, Synergistic effect of graphene oxide@ phosphate-intercalated hydrotalcite for improved anti-corrosion and self-healable protection of waterborne epoxy coating in salt environments, Journal of Materials Chemistry C, 7 (2019) 2318-2326.

[7] H. Huang, X. Sheng, Y. Tian, L. Zhang, Y. Chen, X. Zhang, Two-Dimensional Nanomaterials for Anticorrosive Polymeric Coatings: A Review, Industrial & Engineering Chemistry Research, 59 (2020) 15424-15446.

[8] R. Ding, Y. Zheng, H. Yu, W. Li, X. Wang, T. Gui, Study of water permeation dynamics and anti-corrosion mechanism of graphene/zinc coatings, Journal of Alloys and Compounds, 748 (2018) 481-495.

[9] R. Ding, S. Chen, N. Zhou, Y. Zheng, B.-j. Li, T.-j. Gui, X. Wang, W.-h. Li, H.-b. Yu, H.-w. Tian, The diffusion-dynamical and electrochemical effect mechanism of oriented magnetic graphene on zinc-rich coatings and the electrodynamics and quantum mechanics mechanism of electron conduction in graphene zinc-rich coatings, Journal of Alloys and Compounds, 784 (2019) 756-768.

[10] Q. Zhu, E. Li, X. Liu, W. Song, Y. Li, X. Wang, C. Liu, Epoxy coating with in-situ synthesis of polypyrrole functionalized graphene oxide for enhanced anticorrosive performance, Progress in Organic Coatings, 140 (2020) 105488.

[11] Z. Li, J. Li, J. Cui, H. Qiu, G. Yang, S. Zheng, J. Yang, Dispersion and parallel assembly of sulfonated graphene in waterborne epoxy anticorrosion coatings, Journal of Materials Chemistry A, 7 (2019) 17937-17946.

[12] H. Huang, Y. Tian, Y. Xie, R. Mo, J. Hu, M. Li, X. Sheng, X. Jiang, X. Zhang, Modification of graphene oxide with acrylate phosphorus monomer via thiol-Michael addition click reaction to enhance the anti-corrosive performance of waterborne epoxy coatings, Progress in Organic Coatings, 146 (2020) 105724.

[13] X. Sheng, W. Cai, L. Zhong, D. Xie, X. Zhang, Synthesis of functionalized graphene/polyaniline nanocomposites with effective synergistic reinforcement on anticorrosion, Industrial & Engineering Chemistry Research, 55 (2016) 8576-8585.

[14] S. Wang, Z. Hu, J. Shi, G. Chen, Q. Zhang, Z. Weng, K. Wu, M. Lu, Green synthesis of graphene with the assistance of modified lignin and its application in anticorrosive waterborne epoxy coatings, Applied Surface Science, 484 (2019) 759-770.

[15] X. Lv, X. Li, N. Li, H. Zhang, Y.-z. Zheng, J. Wu, X. Tao, ZrO2 nanoparticle encapsulation of graphene microsheets for enhancing anticorrosion performance of epoxy coatings, Surface and Coatings

Technology, 358 (2019) 443-451.
[16] S. Asaldoust, B. Ramezanzadeh, Synthesis and characterization of a high-quality nanocontainer based on benzimidazole-zinc phosphate (ZP-BIM) tailored graphene oxides; a facile approach to fabricating a smart self-healing anti-corrosion system, Journal of Colloid and Interface Science, 564 (2020) 230-244.
[17] S. Amrollahi, B. Ramezanzadeh, H. Yari, M. Ramezanzadeh, M. Mahdavian, In-situ growth of ceria nanoparticles on graphene oxide nanoplatelets to be used as a multifunctional (UV shield/radical scavenger/anticorrosive) hybrid compound for exterior coatings, Progress in Organic Coatings, 136 (2019) 105241.
[18] S. Asaldoust, M.S. Hosseini, B. Ramezanzadeh, G. Bahlakeh, Construction of a unique anti-corrosion nanocomposite based on Graphene oxide@ Zn3PO4/Epoxy; Experimental characterization and detailed-theoretical quantum mechanics (QM) investigations, Construction and Building Materials, (2020) 119439.
[19] W. Sun, L. Wang, T. Wu, Y. Pan, G. Liu, Inhibited corrosion-promotion activity of graphene encapsulated in nanosized silicon oxide, Journal of Materials Chemistry A, 3 (2015) 16843-16848.
[20] W. Liu, K. Yin, F. He, Q. Ru, S. Zuo, C. Yao, A highly efficient reduced graphene oxide/SnO2/TiO2 composite as photoanode for photocathodic protection of 304 stainless steel, Materials Research Bulletin, 113 (2019) 6-13.
[21] Y. Mai, F. Chen, W. Lian, L. Zhang, C. Liu, X. Jie, Preparation and tribological behavior of copper matrix composites reinforced with nickel nanoparticles anchored graphene nanosheets, Journal of Alloys and Compounds, 756 (2018) 1-7.
[22] S. Vanithakumari, G. Jena, S. Sofia, C. Thinaharan, R. George, J. Philip, Fabrication of superhydrophobic titanium surfaces with superior antibacterial properties using graphene oxide and silanized silica nanoparticles, Surface and Coatings Technology, (2020) 126074.
[23] Z. Liu, S. Tian, Q. Li, J. Wang, J. Pu, G. Wang, W. Zhao, F. Feng, J. Qin, L. Ren, Integrated Dual-Functional ORMOSIL Coatings with AgNPs@ rGO Nanocomposite for Corrosion Resistance and Antifouling Applications, ACS Sustainable Chemistry & Engineering, 8 (2020) 6786-6797.
[24] Z.-R. Yu, S.-N. Li, J. Zang, M. Zhang, L.-X. Gong, P. Song, L. Zhao, G.-D. Zhang, L.-C. Tang, Enhanced mechanical property and flame resistance of graphene oxide nanocomposite paper modified with functionalized silica nanoparticles, Composites Part B: Engineering, 177 (2019) 107347.
[25] C. Liu, H. Zhao, P. Hou, B. Qian, X. Wang, C. Guo, L. Wang, Efficient graphene/cyclodextrin-based nanocontainer: synthesis and host–guest inclusion for self-healing anticorrosion application, ACS applied materials & interfaces, 10 (2018) 36229-36239.
[26] E. Shchukina, D.G. Shchukin, Nanocontainer-based active systems: From self-healing coatings to thermal energy storage, Langmuir, 35 (2019) 8603-8611.
[27] M. Shao, C. Chang, Z. Liu, K. Chen, Y. Zhou, G. Zheng, Z. Huang, H. Xu, P. Xu, B. Lu, Polydopamine coated hollow mesoporous silica nanoparticles as pH-sensitive nanocarriers for overcoming multidrug resistance, Colloids and Surfaces B: Biointerfaces, 183 (2019) 110427.
[28] R.A. Mitran, D. Berger, C. Munteanu, C. Matei, Evaluation of different mesoporous silica supports for energy storage in shape-stabilized phase change materials with dual thermal responses, The Journal of Physical Chemistry C, 119 (2015) 15177-15184.
[29] T. Qian, J. Li, X. Min, B. Fan, Integration of pore confinement and hydrogen-bond influence on the crystallization behavior of C18 PCMs in mesoporous silica for form-stable phase change materials, ACS Sustainable Chemistry & Engineering, 6 (2018) 897-908.

[30] M. Michailidis, E. Gutner-Hoch, R. Wengier, R. Onderwater, R.A. D'Sa, Y. Benayahu, A. Semenov, V. Vinokurov, D.G. Shchukin, Highly Effective Functionalised Coatings with Antibacterial and Antifouling Properties, ACS Sustainable Chemistry & Engineering, (2020).
[31] N. Fatah, S. Triwahyono, A. Jalil, A. Ahmad, T. Abdullah, n-Heptane isomerization over mesostructured silica nanoparticles (MSN): Dissociative-adsorption of molecular hydrogen on Pt and Mo sites, Applied Catalysis A: General, 516 (2016) 135-143.
[32] B. Qian, M. Michailidis, M. Bilton, T. Hobson, Z. Zheng, D. Shchukin, Tannic complexes coated nanocontainers for controlled release of corrosion inhibitors in self-healing coatings, Electrochimica Acta, 297 (2019) 1035-1041.
[33] C. Zea, R. Barranco-García, J. Alcántara, B. Chico, M. Morcillo, D. de la Fuente, Hollow mesoporous silica nanoparticles loaded with phosphomolybdate as smart anticorrosive pigment, Journal of Coatings Technology and Research, 14 (2017) 869-878.
[34] C. Zhou, Z. Li, J. Li, T. Yuan, B. Chen, X. Ma, D. Jiang, X. Luo, D. Chen, Y. Liu, Epoxy composite coating with excellent anticorrosion and self-healing performances based on multifunctional zeolitic imidazolate framework derived nanocontainers, Chemical Engineering Journal, 385 (2020) 123835.
[35] J. Wen, J. Lei, J. Chen, L. Liu, X. Zhang, L. Li, Polyethylenimine wrapped mesoporous silica loaded benzotriazole with high pH-sensitivity for assembling self-healing anti-corrosive coatings, Materials Chemistry and Physics, (2020) 123425.
[36] T. Wang, J. Du, S. Ye, L. Tan, J. Fu, Triple-stimuli-responsive smart nanocontainers enhanced self-healing anticorrosion coatings for protection of aluminum alloy, ACS applied materials & interfaces, 11 (2019) 4425-4438.
[37] W. Wang, H. Wang, J. Zhao, X. Wang, C. Xiong, L. Song, R. Ding, P. Han, W. Li, Self-healing performance and corrosion resistance of graphene oxide–mesoporous silicon layer–nanosphere structure coating under marine alternating hydrostatic pressure, Chemical Engineering Journal, 361 (2019) 792-804.
[38] P. Du, J. Wang, H. Zhao, G. Liu, L. Wang, Graphene oxide encapsulated by mesoporous silica for intelligent anticorrosive coating: studies on release models and self-healing ability, Dalton Transactions, 48 (2019) 13064-13073.
[39] L. Xiong, J. Liu, Y. Li, S. Li, M. Yu, Enhancing corrosion protection properties of sol-gel coating by pH-responsive amino-silane functionalized graphene oxide-mesoporous silica nanosheets, Progress in Organic Coatings, 135 (2019) 228-239.
[40] A. Habibiyan, B. Ramezanzadeh, M. Mahdavian, M. Kasaeian, Facile size and chemistry-controlled synthesis of mussel-inspired bio-polymers based on Polydopamine Nanospheres: Application as eco-friendly corrosion inhibitors for mild steel against aqueous acidic solution, Journal of Molecular Liquids, 298 (2020) 111974.
[41] H. Qian, M. Li, Z. Li, Y. Lou, L. Huang, D. Zhang, D. Xu, C. Du, L. Lu, J. Gao, Mussel-inspired superhydrophobic surfaces with enhanced corrosion resistance and dual-action antibacterial properties, Materials Science and Engineering: C, 80 (2017) 566-577.
[42] Y. Xie, W. Li, H. Huang, D. Dong, X. Zhang, L. Zhang, Y. Chen, X. Sheng, X. Lu, Bio-Based Radish@PDA/PEG Sandwich Composite with High Efficiency Solar Thermal Energy Storage, ACS Sustainable Chemistry & Engineering, 8 (2020) 8448-8457.
[43] C. Liu, Y. Fang, X. Miao, Y. Pei, Y. Yan, W. Xiao, L. Wu, Facile fabrication of superhydrophobic polyurethane sponge towards oil-water separation with exceptional flame-retardant performance, Separation and Purification Technology, 229 (2019) 115801.

[44] H. Huang, M. Li, Y. Tian, Y. Xie, X. Sheng, X. Jiang, X. Zhang, Exfoliation and functionalization of α-zirconium phosphate in one pot for waterborne epoxy coatings with enhanced anticorrosion performance, Progress in Organic Coatings, 138 (2020) 105390.
[45] P. Delparastan, K.G. Malollari, H. Lee, P.B. Messersmith, Direct evidence for the polymeric nature of polydopamine, Angewandte Chemie, 131 (2019) 1089-1094.
[46] B.D.B. Tiu, P. Delparastan, M.R. Ney, M. Gerst, P.B. Messersmith, Cooperativity of Catechols and Amines in High‐Performance Dry/Wet Adhesives, Angewandte Chemie, (2020).
[47] X. Zhang, H. Wang, X. Zhang, Z. Zhao, Y. Zhu, A multifunctional super-hydrophobic coating based on PDA modified MoS_2 with anti-corrosion and wear resistance, Colloids and Surfaces A: Physicochemical and Engineering Aspects, 568 (2019) 239-247.
[48] H. Huang, X. Huang, Y. Xie, Y. Tian, X. Jiang, X. Zhang, Fabrication of h-BN-rGO@PDA nanohybrids for composite coatings with enhanced anticorrosion performance, Progress in Organic Coatings, 130 (2019) 124-131.
[49] B. Qian, Z. Zheng, M. Michailids, N. Fleck, M. Bilton, Y. Song, G. Li, D. Shchukin, Mussel-Inspired Self-Healing Coatings Based on Polydopamine-Coated Nanocontainers for Corrosion Protection, ACS Applied Materials & Interfaces, 11 (2019) 10283-10291.
[50] X. Yang, X. Zhong, J. Zhang, J. Gu, Intrinsic high thermal conductive liquid crystal epoxy film simultaneously combining with excellent intrinsic self-healing performance, Journal of Materials Science & Technology, 68 (2021) 209-215.
[51] A. Habibiyan, B. Ramezanzadeh, M. Mahdavian, G. Bahlakeh, M. Kasaeian, Rational assembly of mussel-inspired polydopamine (PDA)-Zn (II) complex nanospheres on graphene oxide framework tailored for robust self-healing anti-corrosion coatings application, Chemical Engineering Journal, 391 (2020) 123630.
[52] P. Wan, N. Zhao, F. Qi, B. Zhang, H. Xiong, H. Yuan, B. Liao, X. Ouyang, Synthesis of PDA-BN@f-Al_2O_3 hybrid for nanocomposite epoxy coating with superior corrosion protective properties, Progress in Organic Coatings, 146 (2020) 105713.
[53] Y. Zhang, L. Wang, J. Zhang, P. Song, Z. Xiao, C. Liang, H. Qiu, J. Kong, J. Gu, Fabrication and investigation on the ultra-thin and flexible Ti3C2Tx/co-doped polyaniline electromagnetic interference shielding composite films, Composites Science and Technology, 183 (2019) 107833.
[54] Y. Ouyang, L.-X. Li, Z.-H. Xie, L. Tang, F. Wang, C.-J. Zhong, A self-healing coating based on facile pH-responsive nanocontainers for corrosion protection of magnesium alloy, Journal of Magnesium and Alloys, (2020).
[55] L. Wang, L. Chen, P. Song, C. Liang, Y. Lu, H. Qiu, Y. Zhang, J. Kong, J. Gu, Fabrication on the annealed Ti3C2Tx MXene/Epoxy nanocomposites for electromagnetic interference shielding application, Composites Part B: Engineering, 171 (2019) 111-118.